Earth and Planetary Science Letters 494 (2018) 32–41

Contents lists available at ScienceDirect

Earth and Planetary Science Letters

www.elsevier.com/locate/epsl

Magma ascent and lava flow emplacement rates during the 2011 Axial Seamount eruption based on CO_2 degassing

M.R. Jones [a,*], S.A. Soule [b], H.M. Gonnermann [c], V. Le Roux [b], D.A. Clague [d]

[a] Massachusetts Institute of Technology/Woods Hole Oceanographic Institution Joint Program in Oceanography, Woods Hole, MA 02543, USA
[b] Department of Geology and Geophysics, Woods Hole Oceanographic Institution, Woods Hole, MA 02543, USA
[c] Department of Earth, Environmental and Planetary Sciences, Rice University, Houston, TX, 77005, USA
[d] Monterey Bay Aquarium Research Institute, Moss Landing, CA, 95039, USA

ARTICLE INFO

Article history:
Received 23 February 2018
Received in revised form 19 April 2018
Accepted 20 April 2018
Available online 8 May 2018
Editor: T.A. Mather

Keywords:
mid-oceanic ridge basalts
Axial Seamount
eruption mechanisms
lava flow emplacement
submarine volcanism
magma ascent rates
CO_2 in MORB

ABSTRACT

Quantitative metrics for eruption rates at mid-ocean ridges (MORs) would improve our understanding of the structure and formation of the uppermost oceanic crust and would provide a means to link volcanic processes with the conditions of the underlying magmatic system. However, these metrics remain elusive because no MOR eruptions have been directly observed. The possibility of disequilibrium degassing in mid-ocean ridge basalts (MORB), due to high eruptive depressurization rates, makes the analysis of volatile concentrations in MORB glass a promising method for evaluating eruption rates. In this study, we estimate magma ascent and lava flow emplacement rates during the 2011 eruption of Axial Seamount based on numerical modeling of diffusion-controlled bubble growth and new measurements of dissolved volatiles, vesicularity, and vesicle size distributions in erupted basalts. This dataset provides a unique view of the variability in magma ascent (~0.02–1.2 m/s) and lava flow rates (~0.1–0.7 m/s) during a submarine MOR eruption based on 50 samples collected from a >10 km long fissure system and three individual lava flow lobes. Samples from the 2011 eruption display an unprecedented range in dissolved CO_2 concentrations, nearly spanning the full range observed on the global MOR system. The variable vesicularity and dissolved CO_2 concentrations in these samples can be explained by differences in the extent of degassing, dictated by flow lengths and velocities during both vertical ascent and horizontal flow along the seafloor. Our results document, for the first time, the variability in magma ascent rates during a submarine eruption (~0.02–1.2 m/s), which spans the global range previously proposed based on CO_2 degassing. The slowest ascent rates are associated with hummocky flows while faster ascent rates produce channelized sheet flows. This study corroborates degassing-based models for eruption rates using comparisons with independent methods and documents the relationship between eruption dynamics, magma ascent rates, and the morphology of eruptive products. Globally, this approach allows interrogation of the processes that govern mid-ocean ridge eruptions and influence the formation of the oceanic crust.

1. Introduction

Magma ascent and effusion rates exert a strong control on basaltic eruption and emplacement styles, influencing the explosive potential of an eruption, rates of lava flow advance, formation of distributary networks, and morphology of eruptive products. Although several recent mid-ocean ridge (MOR) eruptions have been identified from repeat, high-resolution bathymetric surveys, seafloor instrumentation, post-eruption observations, and radiometric dating (Caress et al., 2012; Chadwick et al., 2016, 1991; Dziak et al., 2009; Fox et al., 2001; Rubin et al., 1994; Soule et al., 2007), no MOR eruption has been directly observed (Rubin et al., 2012). Thus, MOR eruption rates are typically estimated from indirect measures such as seismicity (Dziak et al., 2012, 2007; Tan et al., 2016) and lava flow morphology (Chadwick et al., 2013; Fundis et al., 2010; Gregg and Fink, 1995; Perfit and Chadwick, 1998; Soule et al., 2007). Although seismicity-based methods provide quantitative information about ascent rates (Dziak et al., 2012, 2007) and emplacement rates (Tan et al., 2016), these methods require nearby seafloor instrumentation during the eruption, which is rarely available. Further, lava flow morphology provides only rough estimates of effusion rates; for example, sheet flows are thought to represent higher rates than pil-

* Correspondence to: 360 Woods Hole Road, Woods Hole, MA 02543, USA.
E-mail address: meghanj@mit.edu (M.R. Jones).

https://doi.org/10.1016/j.epsl.2018.04.044
0012-821X/

low lavas (e.g., Gregg and Fink, 1995). Dissolved CO_2 concentrations and vesicle characteristics in erupted basalts may provide a quantitative method for estimating magma ascent and lava flow rates in unobserved eruptions using samples that can be collected long after the eruption has concluded (e.g., Chavrit et al., 2012; Gardner et al., 2016; Soule et al., 2012).

MOR lavas contain measurable dissolved CO_2 at their eruption depth due to CO_2 solubility in basaltic melts and the hydrostatic pressure at the seafloor. Further, high decompression rates commonly lead to incomplete degassing during magma ascent and CO_2 supersaturation in mid-ocean ridge basalts (MORB) relative to expected equilibrium (Dixon et al., 1988; le Roux et al., 2006). The degree of supersaturation depends on the time available for CO_2 diffusion into bubbles, relative to the diffusion time scale, which relates to ascent and flow rates and distances (Chavrit et al., 2012; Dixon et al., 1988; Dixon and Stolper, 1995; Gardner et al., 2016; le Roux et al., 2006; Soule et al., 2012). Based on these principles, Chavrit et al. (2012) suggested that differences in the dissolved CO_2 concentrations and vesicularity characteristics between Atlantic and Pacific MORB result from shorter vertical transport distances and higher ascent rates in Pacific samples. Soule et al. (2012) and Gardner et al. (2016) further demonstrated that two lava flows produced during the 2005–06 East Pacific Rise (EPR) eruption experienced rapid ascent rates (>0.15 m/s) and lava flow rates (0.02–0.12 m/s). Here, we seek to improve methods for interpreting submarine eruptions based on CO_2 degassing by 1) corroborating the model using comparisons with independent methods and 2) establishing the range of ascent rates experienced during a MOR eruption using dissolved CO_2 concentrations and vesicularity, which has not been accessible through other methods.

As the best-monitored submarine volcano in the world, Axial Seamount provides an ideal opportunity to explore the advantages and limitations of degassing-based models for eruption and emplacement processes through comparisons with independent constraints from seismicity and ocean bottom pressure recorders. In this study, we reconstruct magma ascent and lava flow rates (i.e., emplacement rates or flow velocities) during the 2011 Axial Seamount eruption using high-resolution bathymetry (Caress et al., 2012), numerical modeling of CO_2 degassing, and the most comprehensive suite of samples from a single MOR eruption analyzed for volatiles and vesicularity.

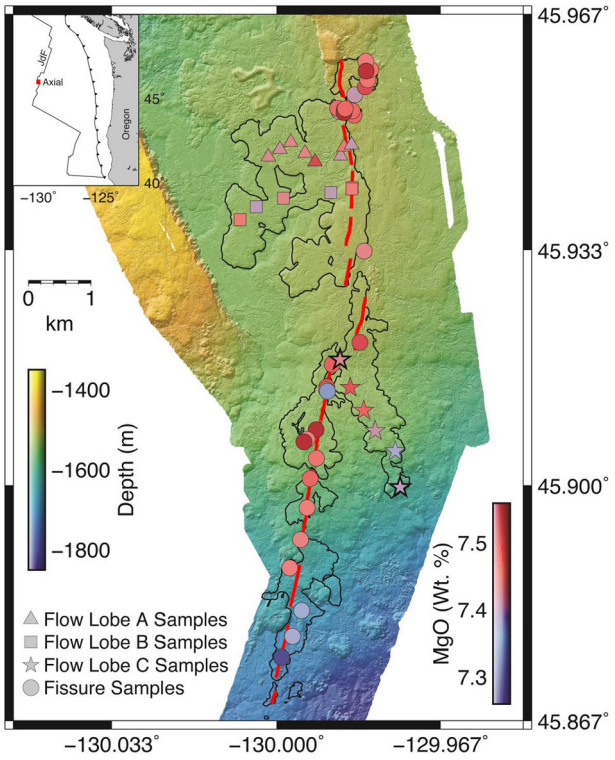

Fig. 1. Map of lava flows emplaced during the 2011 eruption (black outlines, based on Caress et al., 2012 and updated in Clague et al., 2017) showing eruptive fissures (red lines) and lava samples collected from near eruptive fissures (circles) and from individual lava flow lobes extending away from the fissures (Flow Lobe A – triangles, Flow Lobe B – squares, and Flow Lobe C – stars; the flow lobe names are assigned from north to south and do not correspond to a known time progression). Samples are colored according to their MgO content. AUV high-resolution bathymetry is from Clague et al. (2017). Clague et al. (2017) present detailed morphological analyses based on AUV bathymetry and seafloor observations and show that hummocky flows dominate on the upper south rift zone (~45.87°N) while channelized flows dominate from ~45.90°N–45.95°N. Reflected light photomicrographs from two flow lobe C samples, outlined in bold, are shown in Fig. 2. Inset shows the location of Axial Seamount on the Juan de Fuca Ridge (JdF) offshore Oregon. Red box shows the region presented in the main map. (For interpretation of the colors in the figure(s), the reader is referred to the web version of this article.)

2. Axial seamount

Axial Seamount is located ~500 km off the Oregon coast (USA) at the intersection of the Cobb hotspot and the Juan de Fuca Ridge spreading center (Fig. 1). Robust magmatic production at Axial Seamount has resulted in one of the largest and most active, on-axis submarine volcanoes on the global MOR system. This high level of activity has motivated numerous studies about its geology (Clague et al., 2013; Dreyer et al., 2013), morphology (Caress et al., 2012; Chadwick et al., 2013), and associated magma storage (Arnulf et al., 2014; West et al., 2001). The composition of magmas erupted at the summit of Axial Seamount has been mostly bimodal during the last 1000 years, with Group 1 lavas comprising nearly aphyric transitional (T)-MORB with MgO <7.9% and Group 2 lavas comprising plagioclase phyric normal (N)-MORB with MgO >7.9% (Clague et al., 2013; Dreyer et al., 2013).

Axial Seamount has erupted three times during the past 20 years; in 1998 (Chadwick et al., 2013; Fox et al., 2001), in 2011 (Caress et al., 2012; Chadwick et al., 2012; Clague et al., 2017; Dziak et al., 2012), and most recently in 2015 (Chadwick et al., 2016; Nooner and Chadwick, 2016; Wilcock et al., 2016). Bottom pressure recorders and ocean bottom hydrophones revealed patterns in seafloor deformation and seismicity during the 2011 eruption, which were interpreted to represent the onset of diking, followed by the dike breaching the seafloor, followed by lateral, southern dike propagation (Chadwick et al., 2012; Dziak et al., 2012). Chadwick et al. (2016) and Nooner and Chadwick (2016) suggested that diking during the three historic eruptions initiated near the same location, close to the centroid of a best-fit deformation source for the 2015 eruption and near a high-melt conduit identified in multi-channel seismic results from Arnulf et al. (2014).

The distribution of lava flows from the 2011 eruption was identified from pre- and post-eruption 1 m resolution bathymetry acquired using an autonomous underwater vehicle (AUV) (Caress et al., 2012; Clague et al., 2017). The 2011 eruption produced channelized sheet flows on the east rim of the caldera, hummocky flows just south of the channelized flows on the upper south rift zone, and a large, hummocky flow on the lower south rift zone ~30 km south of the caldera (Caress et al., 2012; Clague et al., 2017). The summit lava flows erupted from a series of mostly north-south trending *en echelon* fissures (Caress et al., 2012, Fig. 1).

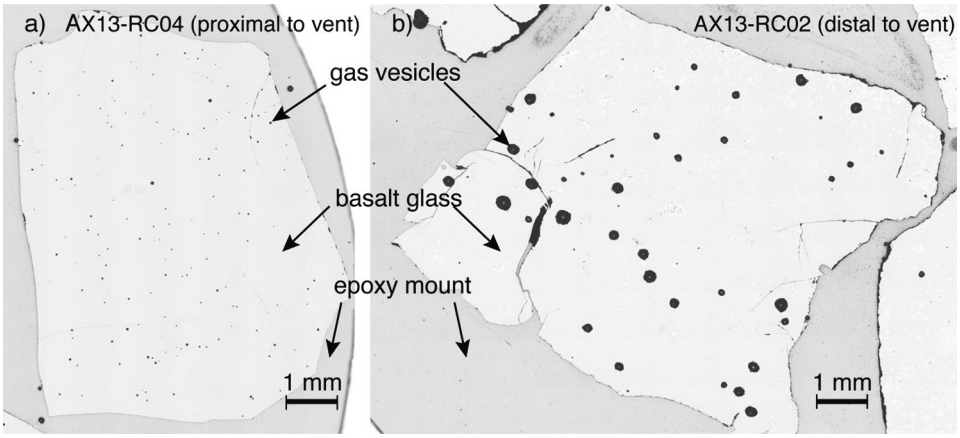

Fig. 2. Reflected-light photomicrographs collected at 10× magnification from samples (a) proximal to eruptive fissures and (b) distal near one flow front terminus from the 2011 eruption. a) Vesicularity in sample AX13-RC04 is 0.51%. b) Vesicularity in sample AX13-RC02 is 1.64%. The outlines for these two samples, collected from flow lobe C, are shown in bold in Fig. 1.

3. Samples and methods

3.1. Sample descriptions

24 lava samples were collected during the VISIONS'11 cruise using the *R/V Thompson* and *ROV ROPOS*. 85 more samples were collected during MBARI's 2011 and 2013 Northern Expeditions using the *R/V Western Flyer*, *ROV Doc Ricketts*, and wax-tipped gravity corers. We analyzed 19 glassy lava samples from VISIONS'11 and 31 samples from the Northern Expeditions. The samples were collected from three large lava flow lobes and along or near the >10 km long series of north-south trending *en echelon* eruptive fissures (Fig. 1). The samples are dominantly aphyric with glassy rinds that were analyzed for major elements, volatiles, vesicularity, and vesicle size distributions.

3.2. Analytical methods

Major elements were analyzed at the University of California at Davis on a 5-spectrometer Cameca SX-100 microprobe (full methods and data in supplementary material S.1). Dissolved volatile concentrations (CO_2, H_2O, F, Cl, S) within the glassy rinds were measured using the Cameca 1280 Secondary Ion Mass Spectrometer at the Northeast National Ion Microprobe Facility (NENIMF) at the Woods Hole Oceanographic Institution using the methods described by Shaw et al. (2010), based on Hauri et al. (2002) (Supplementary Table S.2). Analytical uncertainty ($2\sigma \sim 10\%$) has been established at NENIMF for these procedures based on repeat measurements on standard glass 519-4-1, which agrees with repeat measurements from this study. Helium measurements were conducted on six glass samples using a magnetic sector mass spectrometer at the Isotope Geochemistry Facility at the Woods Hole Oceanographic Institution (Supplementary Table S.3), following methods adapted from Kurz et al. (2005) and described in Soule et al. (2012).

Vesicularities and vesicle size distributions were measured on 10× magnification reflected light photomicrographs of polished glass fragments from the outer quenched 1 cm of the lava samples (Fig. 2, full methods and data in supplementary material S.2). The vesicle number density (number of bubbles per unit volume; N_v) and the vesicle size distributions were derived from the 2D measurements using the stereological methods described in Cashman and Mangan (1994). The vesicle size distributions were interpreted using histograms of bubble density versus bubble size and cumulative bubble volume versus bubble size (Supplementary Material S.4; Shea et al., 2010). The vesicularity, vesicle number density, and vesicle size distributions derived from reflected light photomicrographs agree with those derived from 3D X-ray micro-tomography collected on a subset of the samples (Jones et al., unpublished data).

3.3. Bubble growth model

The numerical formulation used here was first presented for magmatic systems by Prousevitch et al. (1993) and closely follows Arefmanesh and Advani (1991). The model was adapted from single component (H_2O) to multicomponent (H_2O and CO_2) degassing by Gonnermann and Manga (2005). The model simulates gas diffusion within a melt shell, gas exsolution into a bubble, and the associated bubble growth. The model assumes that bubbles are uniformly distributed, such that each bubble can be approximated as a sphere surrounded by a spherical melt shell. The thickness of the melt shell is dictated by the bubble number density. Dissolved volatiles are initially at equilibrium with the exsolved phase and homogeneously distributed throughout the radially symmetrical melt shell. During depressurization, the reduced solubility of the volatile species induces diffusion of the gas from the surrounding melt towards the bubble–melt interface. Bubble growth occurs as dissolved volatiles pass through the bubble–melt interface into the supercritical fluid state. Initial conditions for the model include the initial bubble radius, initial volatile content in the melt, initial pressure, and bubble number density, which are all derived from observations of Axial Seamount 2011 lava samples (Section 5.1). Known parameters include diffusivity (Zhang, 2010), solubility (Dixon et al., 1995; Newman and Lowenstern, 2002), and viscosity (Hui and Zhang, 2007). The unknown parameters are the decompression rate and the degassing timescale after decompression (i.e., while on the seafloor). We estimate decompression rates (Section 5.2) and degassing timescales after decompression (Section 5.3) by comparing model predictions for the dissolved CO_2 concentration and vesicularity with observations from the 2011 Axial samples. Because CO_2 concentrations were measured far from bubbles, we compare these to modeled concentrations at the midpoint between bubbles.

4. Results

4.1. Major elements

Lavas emplaced in the summit caldera during the 2011 eruption are slightly enriched MORB with $CaO/Al_2O_3 = 0.82–0.86$ and $K_2O/Ti_2O = 0.10–0.13$ (Supplementary Table S.1). The samples exhibit a narrow range in major elements (e.g., $SiO_2 = 49.67–49.99$

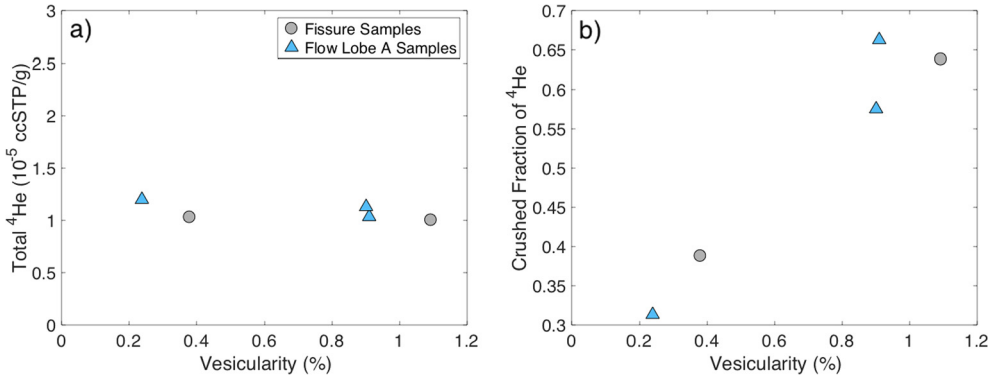

Fig. 3. (a) Total ^{4}He concentration (melting + crushing) versus vesicularity. The limits on the *y*-axis reflect the ranges typically observed in MORB (e.g., Sarda and Graham, 1990). (b) Fraction of ^{4}He released by crushing versus vesicularity. The correlation between crushed fraction of ^{4}He and vesicularity and the relatively constant total ^{4}He concentration suggests that closed system degassing occurred during the 2011 eruption.

wt.%, MgO = 7.26–7.56 wt.%, FeO = 10.93–11.30 wt.%, Al_2O_3 = 14.49–14.80 wt.%, CaO = 12.03–12.43 wt.%), and are similar to Group 1 lavas identified in recent eruptions at Axial Seamount (Dreyer et al., 2013).

4.2. Helium

Total helium concentrations (dissolved + exsolved) in the samples are relatively constant at $1.12 \pm 0.16 \times 10^{-5}$ cm^3 ^{4}He/g at standard temperature and pressure (STP) (Fig. 3, Supplementary Material S.3). The fraction of exsolved helium, measured by crushing, correlates positively with vesicularity and inversely with dissolved CO_2 (Fig. 3). The fraction of helium released by crushing also increases with distance along the lava flows from 0.39 near the vent to 0.66 at the distal end of the flow. Accordingly, the concentration of ^{4}He in the dissolved phase decreases with distance along the lava flows. The ^{3}He/^{4}He ratios derived from crushing and melting range from 8.12–8.33 and are consistent with the typical range of MORB values (Graham, 2002).

4.3. Dissolved volatile concentrations

The dissolved volatile concentrations are within the ranges typical of MORB (H_2O = 0.17–0.26 wt.%, CO_2 = 68–339 ppm where ppm is μg.g^{-1}, F = 125–177 ppm, Cl = 119–196 ppm, and S = 0.096–0.137 wt.%) (Supplementary Table S.2; Wallace et al., 2015). The minor variability in H_2O exceeds the analytical uncertainty, but does not correlate with vesicularity, distance along individual lava flows, or location along the rift zone.

Dissolved CO_2 concentrations span nearly the range of values in lava samples from the global MOR system (Le Voyer et al., 2017; Soule et al., 2012). Distinct variations in dissolved CO_2 are observed in samples collected along the eruptive fissures, with concentrations in southern samples (i.e., 45.875–45.893°N) ranging from ~70 to ~140 ppm, central samples (i.e., 45.894–45.953°N) ranging from ~120 to ~325 ppm, and northern samples (i.e., 45.954–45.961°N) ranging from ~130 to ~180 ppm (Fig. 4c). Dissolved CO_2 concentration decreases systematically with distance along lava flows from ~325 ppm in samples proximal to the eruptive fissures to ~100 ppm in distal samples near the flow terminus (Fig. 4d).

4.4. Vesicularities and vesicle size distributions

Vesicularity ranges from 0.07% to 1.64% (Supplementary Table S.2). Vesicularity varies systematically with location along the eruptive fissures, with the lowest vesicularities observed in the central samples, in the vicinity of the flow lobes A, B, and C (Fig. 4a). Vesicularity also increases with distance from the eruptive fissures (Fig. 4b) and exhibits a negative, linear correlation with dissolved CO_2 concentration and dissolved helium (e.g. Fig. 5), but does not correlate with other volatiles.

Bubble number density (N_v) also varies systematically along the eruptive fissure and individual lava flow units. Along the eruptive fissures, the most northern and southern samples have the lowest N_v (~50–100 bubbles/mm^3), whereas central samples are more variable and have on average higher N_v, ranging from 50–325 bubbles/mm^3 (Fig. 4e). N_v decreases with distance along individual lava flows from ~250 bubbles/mm^3 near the eruptive vents to ~20 bubbles/mm^3 near the flow terminus (Fig. 4f).

R_{max}, defined as the mean radius of the largest bubbles comprising 80% of the total vesicularity, correlates with vesicularity. R_{max} provides a means for evaluating bubble growth independently of detection limits at small sizes. R_{max} varies along the eruptive fissures with the largest R_{max} (~200 μm) at the northern and southern ends and the smallest values (20–80 μm) in the central fissure section (Fig. 4g). R_{max} also increases with distance along the individual lava flows from ~20 μm in samples proximal to eruptive vents to ~140 μm in distal samples (Fig. 4h).

4.5. Total volatile content

Based on empirical solubility models (Dixon and Stolper, 1995), we expect that the vesicles contain >98% CO_2. Total CO_2 concentrations (exsolved + dissolved) in the 2011 samples are relatively constant at 367 ± 30 ppm (uncertainty is 1σ), based on measured dissolved concentrations and calculated exsolved concentrations using sample vesicularity, collection pressure, magmatic temperature (~1200 °C), and a modified Redlich–Kwong equation of state (Flowers, 1979).

5. Discussion

5.1. Degassing during the 2011 Axial Seamount eruption

The relative similarity in total (dissolved + exsolved) ^{4}He and CO_2 concentrations support the assumption that degassing occurred within a closed system (Fig. 3), because progressive bubble loss during open system degassing would produce a positive correlation between total volatile content and the degree of supersaturation. In other words, gas did not escape from the lava during ascent or flow on the seafloor. The constant total volatile concentration among the samples further suggests homogeneous volatile content in the magma prior to eruption.

Based on these observations, we model closed-system degassing of CO_2 into growing bubbles assuming a constant initial

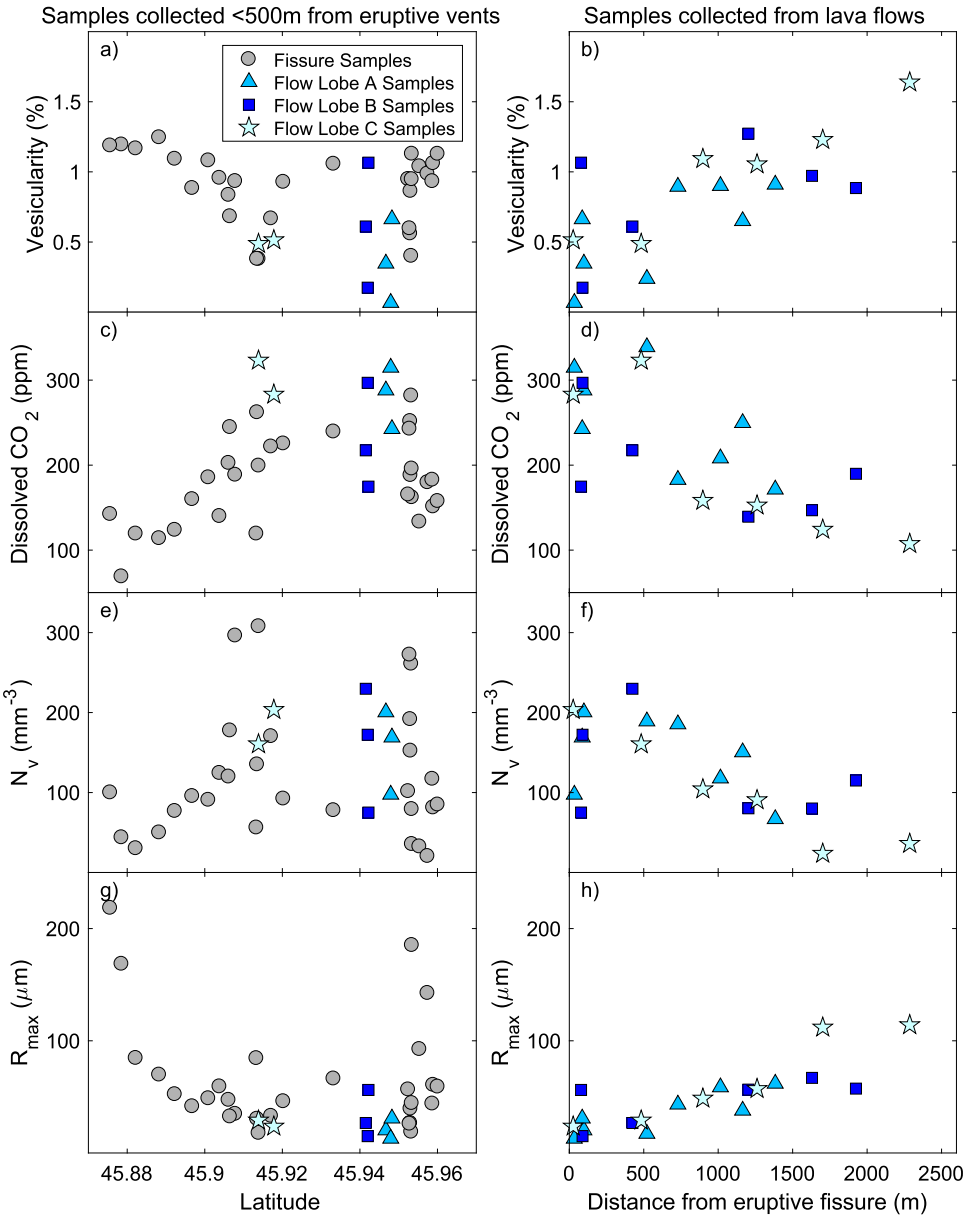

Fig. 4. Vesicularity (a, b), dissolved CO_2 concentrations (c, d), bubble number densities (N_v) (e, f), and characteristic bubble radii (R_{max}) (g, h) in samples from the 2011 eruption of Axial Seamount. Samples collected <500 m from eruptive fissures are plotted versus latitude (left column). Samples collected from individual lava flow lobes are plotted versus distance from the eruptive fissures (right column). Samples from the central fissure section (i.e., 45.894–45.953°N) display lower average vesicularities, higher average dissolved CO_2, higher average N_v, and lower average R_{max} than samples from the southern and northern fissure sections. Vesicularity and R_{max} in samples collected from individual lava flow lobes increases linearly with distance from the fissures, while N_v and dissolved CO_2 decreases linearly with distance from eruptive fissures.

volatile content in all cases. We infer that samples with nearly 0% vesicularity experienced rapid ascent and emplacement with insufficient time for CO_2 diffusion into bubbles; therefore, the dissolved CO_2 concentration in these samples should closely approximate the initial concentration in 2011 Axial Seamount lavas. Thus, we use the volatile concentrations of these samples (0.208 ± 0.008 wt.% H_2O and 325 ± 9 ppm CO_2; e.g. Fig. 5) as the initial condition for our degassing model. We assume that most of the initial CO_2 was dissolved in the melt at the onset of the eruption. Therefore, we use the saturation pressure derived from the inferred initial dissolved CO_2 and H_2O contents (~70 Pa) as an initial condition for the model (Newman and Lowenstern, 2002). Our estimated initial pressure corresponds to a depth of 2.0 km beneath the seafloor, assuming an average seawater density of 1.03 g/cm^3 and an average crustal density of 2.8 g/cm^3, which lies within the depth range of the magma reservoir inferred from multichannel seismic results (1.1–2.3 km between the seafloor and the top of the magmatic reservoir; 0.6–1 km maximum reservoir thickness; Arnulf et al., 2014).

The vesicle volume distributions (supplementary material S.4) demonstrate that small bubbles (<10 μm radius) contain only a minor fraction of the exsolved gas, implying that bubble nucleation had a negligible impact on degassing. Instead, the positive correlation between R_{max} and vesicularity (Fig. 4a, g) indicates that degassing instead occurred primarily through gas exsolution into growing bubbles. The predominantly linear vesicle size distributions (supplementary material S.4) suggest that the correlation between R_{max} and vesicularity results from bubble growth rather than coalescence. Therefore, we neglect bubble nucleation in our model and use measured bubble number densities as an initial condition for our model. We assume initial bubble radii of ~5 μm, based on the smallest resolvable bubble size in these samples. The

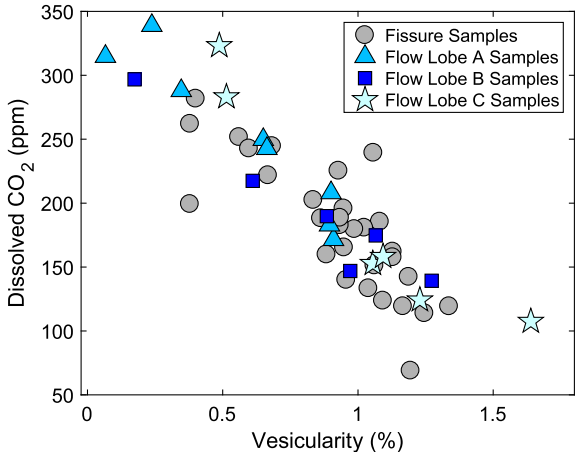

Fig. 5. Dissolved CO_2 concentration versus vesicularity. The inverse correlation suggests that progressive CO_2 degassing due to diffusion leads to the observed variability in dissolved CO_2 concentration and vesicularity. The initial CO_2 concentration for our model was determined as the y-intercept of a linear least-squares regression of the dissolved CO_2 concentration on vesicularity.

assumed sphericity and uniform spacing between vesicles in our model conforms to observations of vesicles in the samples (e.g. Fig. 2).

Solubility models for H_2O and CO_2 (Dixon et al., 1995), and the lack of correlation between vesicularity and H_2O or S suggest that CO_2 was the primary exsolving species. We interpret that the minor variability in H_2O may instead be related to pre-eruption assimilation of seawater derived brines (e.g. le Roux et al., 2006; Soule et al., 2012). Although included in the model, H_2O degassing was negligible.

The variable degree of CO_2 supersaturation, relative to ~65 ppm dissolved CO_2 expected at Axial Seamount seafloor pressures (Dixon and Stolper, 1995), in fissure samples and the progressive decrease in CO_2 supersaturation with distance from the eruptive fissures (Fig. 4c, d) indicate that degassing occurred during both vertical magma ascent and horizontal lava flow across the seafloor. In order to evaluate magma ascent rates for near-fissure samples, we model degassing at various decompression rates and bubble number densities (Section 5.2, Fig. 6). The decompression rate that most closely reproduces the measured dissolved CO_2 concentrations and vesicularity, given the measured bubble number density, provides an estimate for the average ascent rate between the onset of decompression and the lava quenching on the seafloor.

As lava lobe samples proximal to the eruptive vents contain high dissolved CO_2 concentrations and low vesicularities (Fig. 4b, d), we infer that the lavas producing the flows experienced minimal degassing during vertical ascent. In order to evaluate lava flow rates for samples collected from flow lobes A–C, we therefore model degassing at a constant pressure of 15 MPa (equivalent to the hydrostatic pressure at the seafloor) from initial dissolved concentrations of 325 ppm CO_2 and 0.208 wt.% H_2O for the range of measured bubble number densities (Fig. 7). The amount of time available for degassing was estimated by comparing measured dissolved CO_2 concentrations and vesicularity with model results using the observed bubble number densities. The average lava flow rates were calculated from the modeled timescale for degassing and measured flow distance (Section 5.3).

5.2. Degassing during magma ascent

The ascent rates that produce the observed vesicularities and dissolved CO_2 range from ~0.02–1.2 m/s (Fig. 8a), which spans the global range previously proposed based on CO_2 degassing (Chavrit et al., 2012). These ascent rates represent minimum values because the samples probably experienced some degassing while on the seafloor. The high vesicularities, low dissolved CO_2 concentrations, and large bubble radii in samples from the most northern and southern parts of the fissure (Fig. 4b, d, h) suggest that they ascended slower (<0.2 m/s) than samples erupted along the central parts (<1.2 m/s) (Fig. 8a). The greater variability in vesicularity and dissolved CO_2 concentrations in samples from the central parts of the fissure system could reflect complexities in the emplacement dynamics (e.g., pooling in lava ponds) or changes in eruption rate over time, perhaps due to changing pressure conditions within the storage reservoir (Harris et al., 2000; Rivalta, 2010).

Seismicity- and deformation-based methods provide an estimate for initial magma ascent rates during dike propagation, based on the time difference between the initiation of magma ascent, inferred from a pre-eruption earthquake swarm, and the dike breaching the seafloor, inferred from the onset of seafloor deflation (~0.16–0.21 m/s, Dziak et al., 2012). Those estimates are within the range of our modeled ascent rates (~0.02–1.2 m/s); our estimates are slightly more variable because CO_2 degassing records the variability in ascent rates throughout the eruption.

Bottom pressure inflation/deflation records suggest that the dike breached the surface near the north end of the eruptive vents and propagated southward (Chadwick et al., 2012). Based on our study, the lavas emplaced near where the dike first reached the

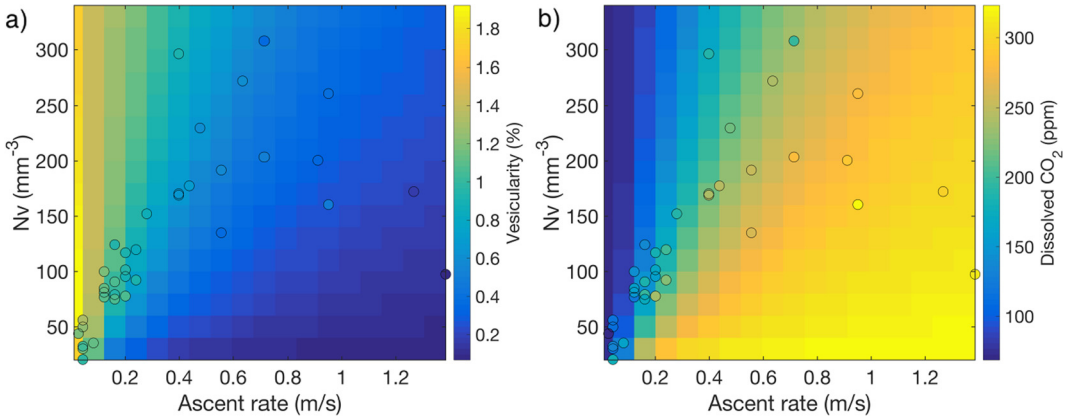

Fig. 6. Results from numerical modeling of diffusive bubble growth during depressurization. (a) Modeled vesicularity and (b) modeled dissolved CO_2 concentration for various bubble number densities (N_v) and depressurization rates. The circles show modeled ascent rates (x-axis), measured N_v (y-axis), measured vesicularity (symbol color on left panel), and measured dissolved CO_2 content (symbol color on right panel) for samples collected <500 m from the fissures. The ascent rates were estimated from the average of the best-fit results for measured dissolved CO_2 concentration and vesicularity.

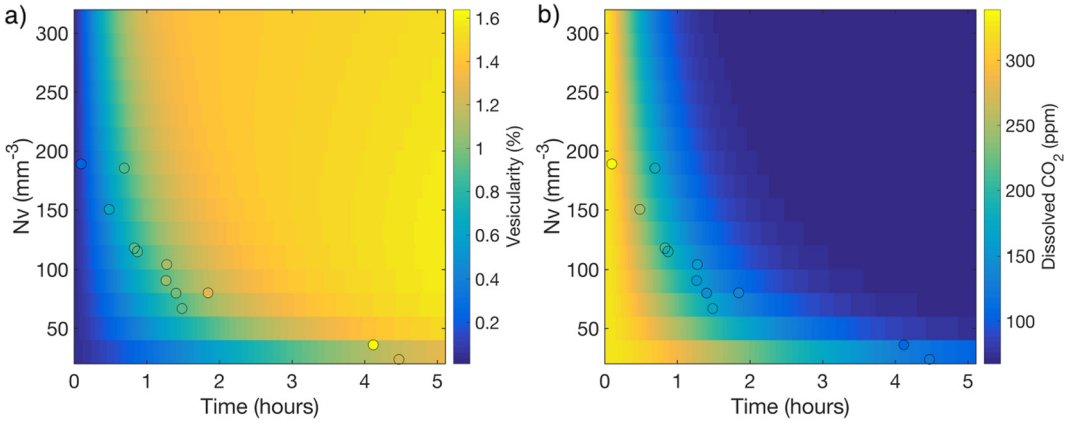

Fig. 7. Results from numerical modeling of diffusive bubble growth during lava flow emplacement. (a) Modeled vesicularity and (b) dissolved CO_2 concentration for various bubble number densities (N_v) and emplacement times. The circles show modeled flow emplacement times (x-axis), measured N_v (y-axis), measured vesicularity (symbol color on left panel), and measured dissolved CO_2 content (symbol color on right panel) for samples collected >500 m from the fissures. The flow emplacement times were estimated from the average of the best-fit results for measured dissolved CO_2 concentration and vesicularity. The flow emplacement rates are estimated from the distance traveled along the seafloor and the amount of time necessary to produce the observed vesicularities and dissolved CO_2 concentrations.

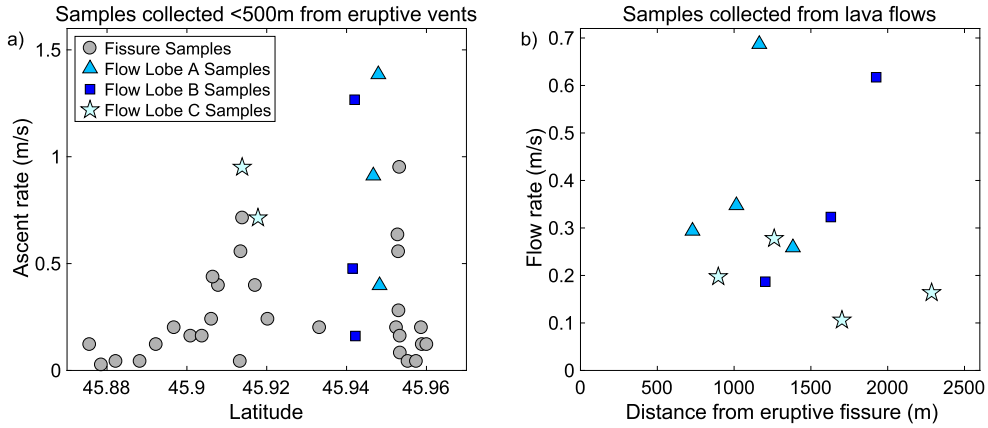

Fig. 8. (a) Magma ascent rates for samples <500 m from eruptive fissures and (b) lava flow emplacement rates for samples >500 m from eruptive fissures based on comparisons between measured CO_2 concentrations, vesicularities and model results.

surface (~45.94°N) experienced the fastest ascent rates, possibly due to high driving overpressures early in the eruption. Slower ascent rates for the northern and southern samples are consistent with lateral dike propagation resulting in longer paths to the seafloor and decreased driving pressure (Fig. 9). The fastest ascent rates also occur near the summit channelized sheet flows while slower ascent rates occur near hummocky flows on the upper south rift zone, supporting a link between effusion rate and lava flow morphology (e.g., Gregg and Fink, 1995).

The agreement between degassing-based and seismicity- and deformation-based models of magma ascent at Axial Seamount provides confidence in applying these methods more broadly to MOR eruptions. The results from these two methods are similarly consistent for the 2005–06 East Pacific Rise (EPR) eruption (Dziak et al., 2009; Gardner et al., 2016; Tolstoy et al., 2006).

5.3. Degassing during lava flow emplacement

The time required to produce the observed vesicularities and dissolved CO_2 concentrations during degassing at seafloor pressures of 15.1 MPa ranges from 0.5 to 4.5 h (Fig. 7). The flow rates, calculated from the ratio of the distance between the fissure and sample location and modeled degassing time, range from ~0.1 to 0.7 m/s for samples greater than 500 meters from the eruptive vents (Fig. 8b). We do not consider samples within 500 meters from the eruptive vents due to potential complexities in the transport pathways and emplacement dynamics (e.g., lava ponding) relative to the total distance flowed. The flow rates do not vary systematically with distance, which contrasts with results from the 2005–2006 EPR eruption where flow rates were inferred to peak at 3 times the average rate early in the eruption (Gardner et al., 2016; Soule et al., 2012). During the 2011 Axial Seamount eruption, samples from the distal ends of the lava flows may have not recorded the period of waning effusion rates.

The volume of the channelized flows near the summit along the upper south rift is 28.7 × 10^6 m^3 (3.5 × 10^6 m^3 per km of fissure) based on pre- and post-eruption high-resolution AUV bathymetry (Caress et al., 2012; updated in Clague et al., 2017). The modeled emplacement times (4.5 h for samples near flow lobe C terminus; Fig. 7b) and calculated summit channelized flow volumes yield an average volumetric effusion rate of 0.22 m^3/s per 1-m length of eruptive fissure. This average effusion rate is similar to the average effusion rate of 0.21 m^3/s per 1-m length of eruptive fissure estimated from data recorded by a trapped bottom pressure recorder (BPR) during the 1998 Axial Seamount eruption in the same area of the summit (Fox et al., 2001).

6. Conclusions

Magma ascent and eruption rates reflect the conditions in the underlying magmatic system (e.g., Rivalta, 2010) and influence the style and mechanisms of volcanic deposition (e.g.,

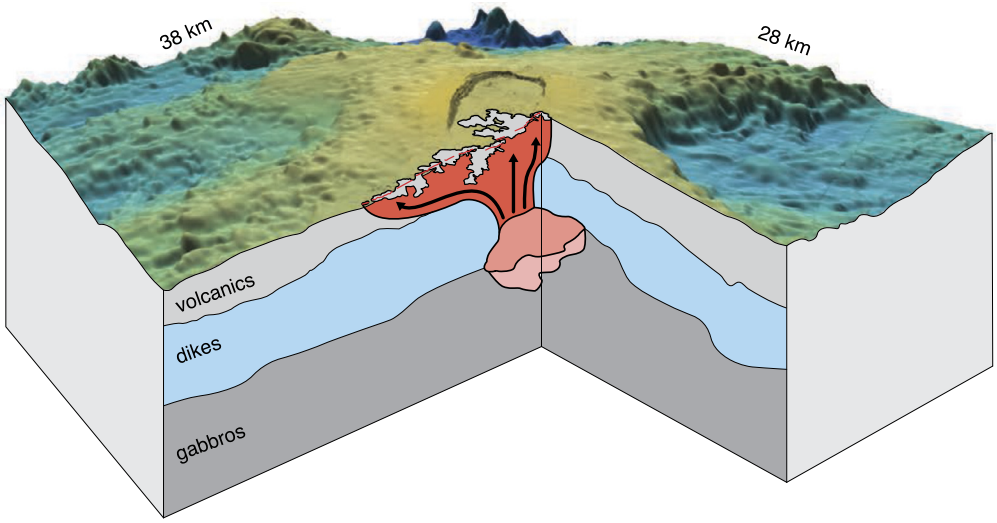

Fig. 9. Schematic representation of the summit portion of the 2011 Axial Seamount eruption based on CO_2 degassing, caldera deformation (Chadwick et al., 2012; Chadwick et al., 2016) and seismicity (Dziak et al., 2012). Lava flow boundaries (black outlines) are based on Caress et al. (2012) and Clague et al. (2017). The subsurface structure is based on Arnulf et al. (2014). High driving overpressures caused rapid decompression rates and minimal degassing in samples from the central portion of the eruption, located above site of dike nucleation for the 2011 and 2015 eruptions (Chadwick et al., 2016), the centroid of the best-fit deformation source for the 2015 eruption (Nooner and Chadwick, 2016), and a high-melt region based on multichannel seismic data (Arnulf et al., 2014). Lateral dike propagation and reduced overpressures produced slower decompression rates, longer ascent paths, and more degassing at the northern and southern ends of the eruptive fissures. Samples collected from lava flows proximal to the vents experienced minimal degassing, based on high dissolved CO_2 concentrations and low vesicularity, indicating the channelized flows are produced by rapid ascent rates. Degassing during flow along the seafloor produced much (~200 ppm) lower dissolved CO_2 concentration in lava flow samples collected near the distal ends of lava flow lobes.

Harris et al., 2000; Gregg and Fink, 1995). In this study, we provide the first quantitative estimates of the variability in magma ascent rates during a single MOR eruption. These ascent rates are sensitive to assumptions regarding the pre-eruptive volatile content and the size distribution of bubbles; however, the result that some samples ascended slow enough for near-equilibrium degassing while others ascended fast enough for minimal vesiculation does not depend on model parameters and holds important implications for our understanding of mid-ocean ridge eruptions. For example, these results, combined with the observation that the fastest ascent rates occur where the dike is thought to have first breached the seafloor, provide the first direct evidence for time-dependent effusion rates during submarine eruptions, similar to that observed during subaerial eruptions (e.g. Harris et al., 2000). In addition, the correspondence between the fastest ascent rates for the 2011 eruption, site of dike nucleation for the 2011 and 2015 eruptions (Chadwick et al., 2016), centroid of the best-fit deformation source for the 2015 eruption (Nooner and Chadwick, 2016), and location of a high-melt nearly vertical conduit in multi-channel seismic data (Arnulf et al., 2014) supports the interpretation that historic, and likely future, eruptions at Axial Seamount initiate near 45.94°N on the east caldera rim (Clague et al., 2017).

This study further supports the relationship between eruption rate and lava flow morphology. The fastest ascent rates (~1.2 m/s), associated with the greatest CO_2 supersaturation, produced channelized flows with sheet morphology from the central fissure section while slower ascent rates are estimated for the southern fissure sections, near hummocky flows and pillow ridges. The ability to evaluate conduit processes in MOR eruptions also holds promise for understanding mechanisms leading to MOR pyroclastic deposits, such as those produced during some Axial Seamount eruptions (Chadwick et al., 2016; Helo et al., 2011).

Our study corroborates degassing-based models for magma ascent and lava flow rates using comparisons with independent estimates from seismicity and caldera deformation. We suggest that degassing-based methods can be applied elsewhere on the MOR system in order to determine global variability in ascent and flow rates and evaluate the processes that control them. Importantly, this method for tracking magma ascent rates relies only on CO_2 supersaturation, which occurs in most MORB (Chavrit et al., 2012), and provides a complementary approach to other diffusion-based chronometers of eruptive processes developed for terrestrial volcanoes (e.g. Lloyd et al., 2014). The observed variability in CO_2 supersaturation within a single eruption demonstrates that sample locations (e.g., relative to eruptive vents) must be well constrained in order to effectively quantify eruption rates using volatile concentrations. With limited direct observations of active eruptions in the deep sea, degassing-based chronometers provide an ideal opportunity to evaluate the archive of eruption dynamics recorded in seafloor volcanic deposits. Our study demonstrates how CO_2 degassing records the physical processes involved in mid-ocean ridge volcanism, including melt storage in the shallow crust, melt extraction during eruptions, and volcanic deposition on the seafloor.

Acknowledgements

We are thankful to the captain and crew of the *R/V Thompson* and *R/V Western Flyer* and the *ROV ROPOS* and *ROV Doc Ricketts* teams for assistance in collecting the samples used in this study. We thank J. Delaney, A. Fundis, and D. Kelley for sample acquisition, B. Dreyer and B. Boulahanis for assistance with sample preparation and processing, D. Wanless and B. Monteleone for assistance with ion probe measurements, M. Kurz and J. Curtice for conducting helium measurements, and N. Botto for conducting microprobe analyses. We thank D. Fornari, T. Grove, D. Lizarralde, M. Kurz, W. Chadwick, and an anonymous reviewer for insightful comments on earlier versions of this manuscript and T. Mather for editorial handling. M. Jones was supported by the Department of Defense (DoD) through the National Defense Science & Engineering Graduate Fellowship (NDSEG) Program. The *ROV Doc Ricketts* sampling and microprobe analysis were supported by a grant from the David and Lucile Packard Foundation to MBARI and the *ROV ROPOS* sampling was supported by the National Science Foundation and the University of Washington. This work was supported by NSF grant OCE-1333492 to A. Soule.

Appendix A. Supplementary material

Supplementary material related to this article can be found online at https://doi.org/10.1016/j.epsl.2018.04.044.

References

Arefmanesh, A., Advani, S., 1991. Diffusion-induced growth of a gas bubble in a viscoelastic fluid. Rheol. Acta 30, 274–283. https://doi.org/10.1007/BF00366641.

Arnulf, A.F., Harding, A.J., Kent, G.M., Carbotte, S.M., Canales, J.P., Nedimovic, M.R., 2014. Anatomy of an active submarine volcano. Geology 42, 655–658. https://doi.org/10.1130/G35629.1.

Caress, D.W., Clague, D.A., Paduan, J.B., Martin, J.F., Dreyer, B.M., Chadwick, W.W., Denny, A., Kelley, D.S., 2012. Repeat bathymetric surveys at 1-metre resolution of lava flows erupted at Axial Seamount in April 2011. Nat. Geosci. 5, 483–488. https://doi.org/10.1038/ngeo1496.

Cashman, K.V., Mangan, M.T., 1994. Physical aspects of magmatic degassing; II, Constraints on vesiculation processes from textural studies of eruptive products. Rev. Mineral. Geochem. 30, 447–478.

Chadwick, W.W., Clague, D.A., Embley, R.W., Perfit, M.R., Butterfield, D.A., Caress, D.W., Paduan, J.B., Martin, J.F., Sasnett, P., Merle, S.G., Bobbitt, A.M., 2013. The 1998 eruption of Axial Seamount: new insights on submarine lava flow emplacement from high-resolution mapping. Geochem. Geophys. Geosyst. 14, 3939–3968. https://doi.org/10.1002/ggge.20202.

Chadwick, W.W., Embley, R.W., Fox, C.G., 1991. Evidence for volcanic eruption on the southern Juan de Fuca ridge between 1981 and 1987. Nature 350, 416–418. https://doi.org/10.1038/350416a0.

Chadwick, W.W., Nooner, S.L., Butterfield, D.A., Lilley, M.D., 2012. Seafloor deformation and forecasts of the April 2011 eruption at Axial Seamount. Nat. Geosci. 5, 474–477. https://doi.org/10.1038/ngeo1464.

Chadwick, W.W., Paduan, J.B., Clague, D.A., Dreyer, B.M., Merle, S.G., Bobbitt, A.M., Caress, D.W., Philip, B.T., Kelley, D.S., Nooner, S.L., 2016. Voluminous eruption from a zoned magma body after an increase in supply rate at Axial Seamount. Geophys. Res. Lett. 43, 12063–12070. https://doi.org/10.1002/2016GL071327.

Chavrit, D., Humler, E., Morizet, Y., Laporte, D., 2012. Influence of magma ascent rate on carbon dioxide degassing at oceanic ridges: message in a bubble. Earth Planet. Sci. Lett. 357–358, 376–385. https://doi.org/10.1016/j.epsl.2012.09.042.

Clague, D., Paduan, J., Caress, D., Chadwick, W., Le Saout, M., Dreyer, B., Portner, R., 2017. High-resolution AUV mapping and targeted ROV observations of three historical lava flows at Axial Seamount. Oceanography 30. https://doi.org/10.5670/oceanog.2017.426.

Clague, D.A., Dreyer, B.M., Paduan, J.B., Martin, J.F., Chadwick, W.W., Caress, D.W., Portner, R.A., Guilderson, T.P., McGann, M.L., Thomas, H., Butterfield, D.A., Embley, R.W., 2013. Geologic history of the summit of Axial Seamount, Juan de Fuca Ridge. Geochem. Geophys. Geosyst. 14, 4403–4443. https://doi.org/10.1002/ggge.20240.

Dixon, J.E., Stolper, E.M., 1995. An experimental study of water and carbon dioxide solubilities in mid-ocean ridge basaltic liquids, part II: applications to degassing. J. Petrol. 36, 1633–1646. https://doi.org/10.1093/oxfordjournals.petrology.a037268.

Dixon, J.E., Stolper, E., Delaney, J.R., 1988. Infrared spectroscopic measurements of CO_2 and H_2O in Juan de Fuca ridge basaltic glasses. Earth Planet. Sci. Lett. 90, 87–104. https://doi.org/10.1016/0012-821X(88)90114-8.

Dixon, J.E., Stolper, E.M., Holloway, J.R., 1995. An experimental study of water and carbon dioxide solubilities in mid-ocean ridge basaltic liquids, part I: calibration and solubility models. J. Petrol. 36, 1607–1631. https://doi.org/10.1093/oxfordjournals.petrology.a037267.

Dreyer, B.M., Clague, D.A., Gill, J.B., 2013. Petrological variability of recent magmatism at Axial Seamount summit, Juan de Fuca Ridge. Geochem. Geophys. Geosyst. 14, 4306–4333. https://doi.org/10.1002/ggge.20239.

Dziak, R.P., Bohnenstiehl, D.R., Cowen, J.P., Baker, E.T., Rubin, K.H., Haxel, J.H., Fowler, M.J., 2007. Rapid dike emplacement leads to eruptions and hydrothermal plume release during seafloor spreading events. Geology 35, 579–582. https://doi.org/10.1130/G23476A.1.

Dziak, R.P., Bohnenstiehl, D.R., Matsumoto, H., Fowler, M.J., Haxel, J.H., Tolstoy, M., Waldhauser, F., 2009. January 2006 seafloor-spreading event at 9°50′N, East Pacific rise: ridge dike intrusion and transform fault interactions from regional hydroacoustic data. Geochem. Geophys. Geosyst. 10, Q06T06. https://doi.org/10.1029/2009GC002388.

Dziak, R.P., Haxel, J.H., Bohnenstiehl, D.R., Chadwick, W.W., Nooner, S.L., Fowler, M.J., Matsumoto, H., Butterfield, D.A., 2012. Seismic precursors and magma ascent before the April 2011 eruption at Axial Seamount. Nat. Geosci. 5, 478–482. https://doi.org/10.1038/ngeo1490.

Flowers, G.C., 1979. Correction of Holloway's (1977) adaptation of the modified Redlich–Kwong equation of state for calculation of the fugacities of molecular species in supercritical fluids of geologic interest. Contrib. Mineral. Petrol. 69, 315–318. https://doi.org/10.1007/BF00372333.

Fox, C.G., Chadwick, W.W., Embley, R.W., 2001. Direct observation of a submarine volcanic eruption from a sea-floor instrument caught in a lava flow. Nature 412, 727–729. https://doi.org/10.1038/35089066.

Fundis, A.T., Soule, S.A., Fornari, D.J., Perfit, M.R., 2010. Paving the seafloor: volcanic emplacement processes during the 2005–2006 eruptions at the fast spreading East Pacific rise, 9°50′N. Geochem. Geophys. Geosyst. 11, Q08024. https://doi.org/10.1029/2010GC003058.

Gardner, J.E., Jackson, B.A., Gonnermann, H., Soule, S.A., 2016. Rapid ascent and emplacement of basaltic lava during the 2005-06 eruption of the East Pacific rise at ca. 9°51′N as inferred from CO_2 contents. Earth Planet. Sci. Lett. 453, 152–160. https://doi.org/10.1016/j.epsl.2016.08.007.

Gonnermann, H.M., Manga, M., 2005. Nonequilibrium magma degassing: results from modeling of the ca. 1340 A.D. eruption of mono craters, California. Earth Planet. Sci. Lett. 238, 1–16. https://doi.org/10.1016/j.epsl.2005.07.021.

Graham, D.W., 2002. Noble gas isotope geochemistry of mid-ocean ridge and ocean island basalts: characterization of mantle source reservoirs. Rev. Mineral. Geochem. 47, 247–317. https://doi.org/10.2138/rmg.2002.47.8.

Gregg, T.K.P., Fink, J.H., 1995. Quantification of submarine lava-flow morphology through analog experiments. Geology 23, 73–76. https://doi.org/10.1130/0091-7613(1995)023<0073:QOSLFM>2.3.CO;2.

Harris, A.J.L., Murray, J.B., Aries, S.E., Davies, M.A., Flynn, L.P., Wooster, M.J., Wright, R., Rothery, D.A., 2000. Effusion rate trends at Etna and Krafla and their implications for eruptive mechanisms. J. Volcanol. Geotherm. Res. 102, 237–269. https://doi.org/10.1016/S0377-0273(00)00190-6.

Hauri, E., Wang, J., Dixon, J.E., King, P.L., Mandeville, C., Newman, S., 2002. SIMS analysis of volatiles in silicate glasses, 1: calibration, matrix effects and comparisons with FTIR. Chem. Geol. 183, 99–114. https://doi.org/10.1016/S0009-2541(01)00375-8. Melt inclusions at the millennium: toward a deeper understanding of magmatic processes.

Helo, C., Longpre, M.-A., Shimizu, N., Clague, D.A., Stix, J., 2011. Explosive eruptions at mid-ocean ridges driven by CO_2-rich magmas. Nat. Geosci. 4, 260–263. https://doi.org/10.1038/NGEO1104.

Hui, H., Zhang, Y., 2007. Toward a general viscosity equation for natural anhydrous and hydrous silicate melts. Geochim. Cosmochim. Acta 71, 403–416. https://doi.org/10.1016/j.gca.2006.09.003.

Kurz, M.D., Moreira, M., Curtice, J., Lott III, D.E., Mahoney, J.J., Sinton, J.M., 2005. Correlated helium, neon, and melt production on the super-fast spreading East Pacific rise near 17°S. Earth Planet. Sci. Lett. 232, 125–142. https://doi.org/10.1016/j.epsl.2005.01.005.

le Roux, P., Shirey, S., Hauri, E., Perfit, M., Bender, J., 2006. The effects of variable sources, processes and contaminants on the composition of northern EPR MORB (8–10°N and 12–14°N): evidence from volatiles (H_2O, CO_2, S) and halogens (F, Cl). Earth Planet. Sci. Lett. 251, 209–231. https://doi.org/10.1016/j.epsl.2006.09.012.

Le Voyer, M., Kelley, K.A., Cottrell, E., Hauri, E.H., 2017. Heterogeneity in mantle carbon content from CO_2-undersaturated basalts. Nat. Commun. 8, 14062. https://doi.org/10.1038/ncomms14062.

Lloyd, A.S., Ruprecht, P., Hauri, E.H., Rose, W., Gonnermann, H.M., Plank, T., 2014. NanoSIMS results from olivine-hosted melt embayments: magma ascent rate during explosive basaltic eruptions. J. Volcanol. Geotherm. Res. 283, 1–18. https://doi.org/10.1016/j.jvolgeores.2014.06.002.

Newman, S., Lowenstern, J.B., 2002. VolatileCalc: a silicate melt–H_2O–CO_2 solution model written in visual basic for excel. Comput. Geosci. 28, 597–604. https://doi.org/10.1016/S0098-3004(01)00081-4.

Nooner, S.L., Chadwick, W.W., 2016. Inflation-predictable behavior and co-eruption deformation at Axial Seamount. Science 354, 1399–1403. https://doi.org/10.1126/science.aah4666.

Perfit, M.R., Chadwick, W.W., 1998. Magmatism at mid-ocean ridges: constraints from volcanological and geochemical investigations. In: Buck, W.R., Delaney, P.T., Karson, J.A., Lagabrielle, Y. (Eds.), Faulting and Magmatism at Mid-Ocean Ridges. American Geophysical Union, pp. 59–115.

Prousevitch, A., Sahagian, D., Anderson, A., 1993. Dynamics of diffusive bubble-growth in magmas – isothermal case. J. Geophys. Res., Solid Earth 98, 22283–22307. https://doi.org/10.1029/93JB02027.

Rivalta, E., 2010. Evidence that coupling to magma chambers controls the volume history and velocity of laterally propagating intrusions. J. Geophys. Res. 115. https://doi.org/10.1029/2009JB006922.

Rubin, K., Soule, S.A., Chadwick, W., Fornari, D., Clague, D., Embley, R., Baker, E., Perfit, M., Caress, D., Dziak, R., 2012. Volcanic eruptions in the deep sea. Oceanography 25, 142–157. https://doi.org/10.5670/oceanog.2012.12.

Rubin, K.H., Macdougall, J.D., Perfit, M.R., 1994. ^{210}Po–^{210}Pb dating of recent volcanic eruptions on the sea floor. Nature 368, 841–844. https://doi.org/10.1038/368841a0.

Sarda, P., Graham, D., 1990. Mid-ocean ridge popping rocks: implications for degassing at ridge crests. Earth Planet. Sci. Lett. 97, 268–289. https://doi.org/10.1016/0012-821X(90)90047-2.

Shaw, A.M., Behn, M.D., Humphris, S.E., Sohn, R.A., Gregg, P.M., 2010. Deep pooling of low degree melts and volatile fluxes at the 85°E segment of the Gakkel ridge: evidence from olivine-hosted melt inclusions and glasses. Earth Planet. Sci. Lett. 289, 311–322. https://doi.org/10.1016/j.epsl.2009.11.018.

Shea, T., Houghton, B.F., Gurioli, L., Cashman, K.V., Hammer, J.E., Hobden, B.J., 2010. Textural studies of vesicles in volcanic rocks: an integrated methodology. J. Volcanol. Geotherm. Res. 190, 271–289. https://doi.org/10.1016/j.jvolgeores.2009.12.003.

Soule, S.A., Fornari, D.J., Perfit, M.R., Rubin, K.H., 2007. New insights into mid-ocean ridge volcanic processes from the 2005–2006 eruption of the East Pacific rise, 9°46'N–9° 56'N. Geology 35, 1079–1082. https://doi.org/10.1130/G23924A.1.

Soule, S.A., Nakata, D.S., Fornari, D.J., Fundis, A.T., Perfit, M.R., Kurz, M.D., 2012. CO_2 variability in mid-ocean ridge basalts from syn-emplacement degassing: constraints on eruption dynamics. Earth Planet. Sci. Lett. 327–328, 39–49. https://doi.org/10.1016/j.epsl.2012.01.034.

Tan, Y.J., Tolstoy, M., Waldhauser, F., Wilcock, W.S.D., 2016. Dynamics of a seafloor-spreading episode at the East Pacific rise. Nature 540, 261–265. https://doi.org/10.1038/nature20116.

Tolstoy, M., Cowen, J.P., Baker, E.T., Fornari, D.J., Rubin, K.H., Shank, T.M., Waldhauser, F., Bohnenstiehl, D.R., Forsyth, D.W., Holmes, R.C., Love, B., Perfit, M.R., Weekly, R.T., Soule, S.A., Glazer, B., 2006. A sea-floor spreading event captured by seismometers. Science 314, 1920–1922. https://doi.org/10.1126/science.1133950.

Wallace, P.J., Plank, T., Edmonds, M., Hauri, E.H., 2015. Volatiles in magmas. In: Sigurdsson, H. (Ed.), The Encyclopedia of Volcanoes, second edition. Academic Press, Amsterdam, pp. 163–183.

West, M., Menke, W., Tolstoy, M., Webb, S., Sohn, R., 2001. Magma storage beneath axial volcano on the Juan de Fuca mid-ocean ridge. Nature 413, 833–836. https://doi.org/10.1038/35101581.

Wilcock, W.S.D., Tolstoy, M., Waldhauser, F., Garcia, C., Tan, Y.J., Bohnenstiehl, D.R., Caplan-Auerbach, J., Dziak, R.P., Arnulf, A.F., Mann, M.E., 2016. Seismic constraints on caldera dynamics from the 2015 Axial Seamount eruption. Science 354, 1395–1399. https://doi.org/10.1126/science.aah5563.

Zhang, Y., 2010. Diffusion of H, C, and O components in silicate melts. Rev. Mineral. Geochem. 72, 171–225. https://doi.org/10.2138/rmg.2010.72.5.